Lawrence Berkeley National Laboratory

LBL Publications

Title

Dynamic circular birefringence response with fractured geometric phase metasurface systems

Permalink

https://escholarship.org/uc/item/78h5q51c

Journal

Proceedings of the National Academy of Sciences of the United States of America, 119(12)

ISSN

0027-8424

Authors

Wang, Evan W

Phan, Thaibao

Yu, Shang-Jie

et al.

Publication Date

2022-03-22

DOI

10.1073/pnas.2122085119

Copyright Information

This work is made available under the terms of a Creative Commons Attribution License, available at https://creativecommons.org/licenses/by/4.0/

Peer reviewed

eScholarship.org Powered by the California Digital Library
University of California

PNAS RESEARCH ARTICLE | ENGINEERING

Dynamic circular birefringence response with fractured geometric phase metasurface systems

Evan W. Wang[a], Thaibao Phan[a], Shang-Jie Yu[a], Scott Dhuey[b], and Jonathan A. Fan[a,1]

Edited by J. Pendry, Imperial College London, London, United Kingdom; received December 6, 2021; accepted February 9, 2022

Control over symmetry breaking in three-dimensional electromagnetic systems offers a pathway to tailoring their optical activity. We introduce fractured Pancharatnam–Berry-phase metasurface systems, in which a full-waveplate geometric phase metasurface is fractured into two half-waveplate-based metasurfaces and actively configured using shear displacement. Local relative rotations between stacked half-nanowaveplates within the metasurface system are transduced by shear displacement, leading to dynamic modulation of their collective geometric phase properties. We apply this concept to pairs of periodic Pancharatnam–Berry-phase metasurfaces and experimentally show that these systems support arbitrary and reconfigurable broadband circular birefringence response. High-speed circular birefringence modulation is demonstrated with modest shearing speeds, indicating the potential for these concepts to dynamically control polarization states with fast temporal responses. We anticipate that fractured geometric phase metasurface systems will serve as a nanophotonic platform that leverages systems-level symmetry breaking to enable active electromagnetic wave control.

metasurface | circular birefringence | polarization rotation | geometric phase | topology optimization

Significance

Optical activity is a fundamental property of symmetry-broken three-dimensional systems and enables control of the polarization state of electromagnetic waves. This work introduces a type of reconfigurable geometric phase response in which shearing displacements between two Pancharatnam–Berry-phase metasurfaces transduce chiral symmetry breaking within nanoscale waveguide structures. These metasurface systems, termed fractured metasurface waveplates, can be tailored to support dynamically tunable, broadband circular birefringence responses. Polarization modulation is based on microscopic motions and uniquely enables high-speed modulation over large area apertures. Our system paves the way for new classes of nanophotonic devices that feature systems-level symmetry breaking for controlling electromagnetic waves, which is relevant for sensing, imaging, and quantum-control applications.

Chirality is an intrinsic symmetry property of three-dimensional systems and arises when the system is distinguishable from its mirror image (1, 2). The light–matter interactions between electromagnetic waves and chiral media are collectively described as optical activity and can be decomposed into two distinct phenomena. The first is circular dichroism, which is characterized by differences in absorption between transmitted right- and left-handed circularly polarized waves (RCP and LCP waves, respectively). The second is circular birefringence, which is characterized by differences in transmitted phase accumulation between RCP and LCP waves. The broad technological implications of chiral media and limited chiro-optical response from naturally occurring materials have spurred the study and development of passive (3–7) and active (8–10) chiral metamaterials, which serve as artificial chiral systems with compact form factors and enhanced responses. The chiral responses from nearly all prior metamaterial demonstrations involve circular dichroism, and engineered circular birefringence systems have only started to be explored recently (11, 12). While engineered circular dichroism can be achieved by maximizing extinction in static systems, the applicability of circular birefringence to polarization control, imaging, sensing, and other applications demands greater flexibility than a single fixed retardance. The difficult task of designing metamaterials with dynamically reconfigurable circular birefringence has not yet been demonstrated.

To this end, dielectric metasurfaces provide a new framework for polarization control (13–16), and metasurfaces based on Pancharatnam–Berry phase are a natural candidate platform for tailoring circular birefringence response because they manipulate light in the circular polarization basis (17–22). Mechanistically, Pancharatnam–Berry-phase metasurfaces are constructed from arrays of subwavelength-scale nanowaveguides, each functioning as half-waveplates. Each nanowaveplate transforms incident RCP light to outgoing LCP light with a phase shift that is proportional to the nanowaveplate rotation angle. These phase variations are a form of geometric phase (*SI Appendix*, section 1), and they can collectively enable wavefront engineering tasks, such as the selective diffraction of circularly polarized waves, which is accomplished in metagratings that feature a periodic gradient in nanowaveplate rotation angle. While Pancharatnam–Berry-phase metasurfaces have been broadly researched, existing manifestations involve single layers of nanostructures, yielding achiral systems that lack the symmetry-breaking properties required for circular birefringence control. In addition, they are static systems and lack the configurable dynamic control required for many applications.

In this letter, we present fractured Pancharatnam–Berry-phase metasurface systems, which can be conceptualized as a full-waveplate geometric phase metasurface that is fractured into two half-waveplate-based metasurfaces (Fig. 1*A*). The full-waveplate system without fracturing is the composition of two aligned half-nanowaveplates that imparts

Author contributions: E.W.W., T.P., and J.A.F. designed research; E.W.W. and T.P. performed research; E.W.W., S.-J.Y., and S.D. contributed new reagents/analytic tools; E.W.W. analyzed data; and E.W.W., S.-J.Y., and J.A.F. wrote the paper.

The authors declare no competing interest.

This article is a PNAS Direct Submission.

Copyright © 2022 the Author(s). Published by PNAS. This article is distributed under Creative Commons Attribution-NonCommercial-NoDerivatives License 4.0 (CC BY-NC-ND).

[1]To whom correspondence may be addressed. Email: jonfan@stanford.com.

This article contains supporting information online at https://www.pnas.org/lookup/suppl/doi:10.1073/pnas.2122085119/-/DCSupplemental.

Published March 16, 2022.

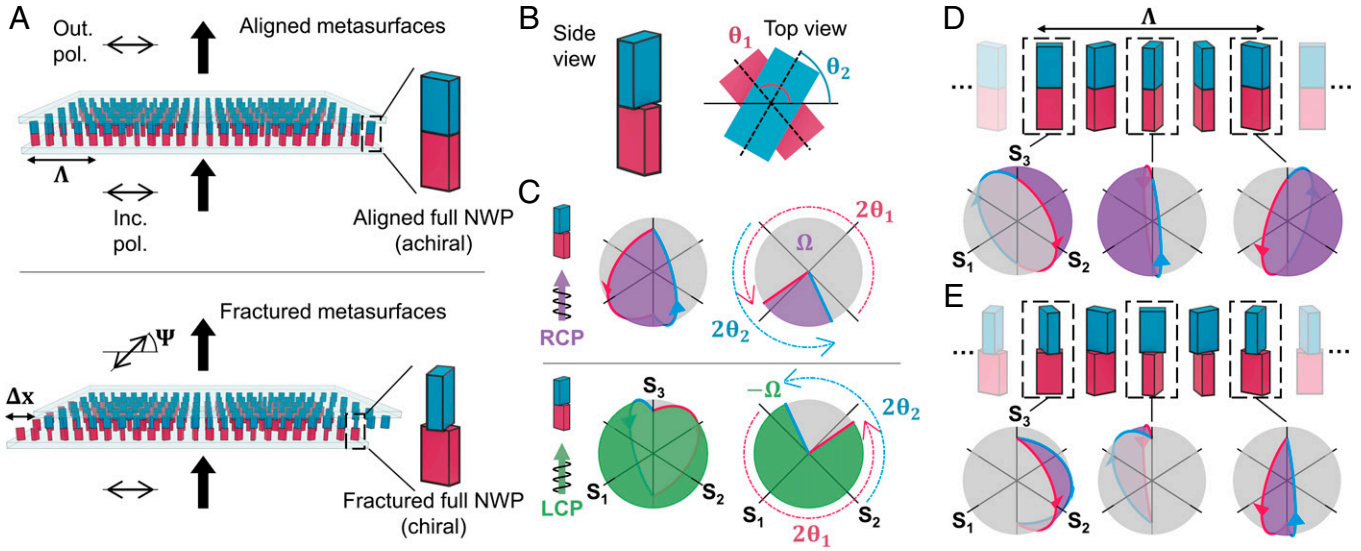

Fig. 1. Metasurface systems with reconfigurable geometric phase response for circular birefringence control. (*A*) Schematic of aligned (*Upper*) and fractured (*Lower*) metasurface systems alongside a representative aligned full nanowaveplate (NWP) and fractured full nanowaveplate, respectively. Incident light passing through the system undergoes a polarization rotation Ψ that is a linear function of the shear displacement Δx between the metagratings. Inc., incident; Out., output; pol., polarization. (*B*) Side (*Left*) and top (*Right*) views of a fractured nanowaveplate. The rotation angles associated with the bottom and top nanowaveplate components use the S_1 axis as a reference and are θ_1 and θ_2, respectively. (*C*) Side (*Left*) and top (*Right*) views of Poincare spheres showing the pathways taken by incident RCP (*Upper*) and LCP (*Lower*) light through the fractured nanowaveplate in *B*. The accumulated geometric phase is denoted by the enclosed shaded area in each sphere. (*D* and *E*) Perfectly aligned (*D*) and fractured (*E*) metasurface systems, together with visualizations of polarization pathways on the Poincare sphere under RCP illumination corresponding to different nanowaveplate configurations.

no net phase response to an incident wave and is achiral, as individual full nanowaveplates possess reflection symmetry. However, as a shear displacement is imparted on the fractured metasurface system, the full nanowaveplates will instead form from two half-nanowaveplate components with differing relative rotation angles, yielding fractured full nanowaveplates that are chiral and possess a nontrivial geometric phase response. The collective Pancharatnam–Berry-phase response of the system therefore derives from two geometric degrees of freedom, the spatial gradient in nanowaveguide angle featured in the full-waveplate system and the relative metasurface displacement in the fractured system, Δx. For periodic Pancharatnam–Berry-phase metasurfaces, or metagratings, shear displacements of the fractured metasurface system transduce local relative rotations in the fractured full nanowaveplates, producing a dynamic circular birefringence response with a polarization rotation angle Ψ. The displacement distance required to produce arbitrary Ψ's is on the order of the metagrating period, Λ, leading to high-speed polarization control based on microscale displacements that can enable new applications in high-speed modulators (23), shutters, polarization-based metrology and display systems (24), and quantum control and readout (25).

Principle

To conceptualize the underlying relationship between symmetry breaking in the metasurface system and its corresponding response to circularly polarized light, we examine the properties of an individual fractured full nanowaveplate in more detail. The bottom and top half-nanowaveplate components have angular orientations θ_1 and θ_2, respectively. The analysis presented here assumes that the nanowaveplate components exhibit ideal half-waveplate behavior, and near-field interactions between the nanowaveplates are neglected. A full-wave treatment of this system is presented in *SI Appendix*, section 2 and shows that the full vectorial electromagnetic behavior of the fractured full nanowaveplate is consistent with the simplified analysis presented here. We note that our use of concentrically aligned nanowaveplates limits Δx in metagrating systems to quantized values, but we will later consider a metasurface system scheme that relieves this constraint. When the relative angle of the fractured full nanowaveplate, $\Delta\theta = \theta_1 - \theta_2$, has values of zero modulo $\pi/2$, it acts as a perfectly symmetric and achiral full waveplate. It is chiral at all other angles with varying degrees of reflection symmetry breaking.

As an incident circularly polarized light beam travels through the fractured full nanowaveplate, the handedness of the outgoing wave remains the same as that of the incident wave and is independent of the angular orientations of the half-nanowaveplate components. However, there exists a relative polarization-dependent phase accumulation that arises from these angular orientations. This phase accumulation takes the form of a geometric phase and can be visualized as an enclosed area on the Poincare sphere (26, 27). Propagation through the fractured full nanowaveplate produces a path along the Poincare sphere that encloses an area with solid angle Ω, as visualized in Fig. 1*C*, and leads to an accumulated Pancharatnam–Berry geometric phase, ϕ, equal to half of the solid angle. The value of this geometric phase is equal and opposite between the two circular polarizations, leading to circular birefringence that scales linearly with the relative angle, $\Delta\theta$, within the fractured waveplate. Interestingly, while circular birefringence depends on the relative orientations of the half-nanowaveplate components, it has no dependence on the absolute angular orientation (i.e., reference axis for θ_1 and θ_2; Fig. 1*B*) of fractured full nanowaveplate. Such behavior is unique to our system, which exhibits matching input and output polarizations and therefore supports geometric phase properties that depend only on the internal geometry of the structure.

Our analysis of fractured full nanowaveplates can be used to understand the chiro-optical properties of our full metasurface system, which comprise an array of such structures with relative and global angular orientations that are a function of Δx. When Δx equals zero, the fractured full nanowaveplates possess $\Delta\theta$ equal to zero and are achiral (Fig. 1*D*). These structures produce the same geometric phase response for incident LCP and RCP waves, and an incident beam interacting with this system

therefore experiences no circular birefringence response. Upon system displacement, the full nanowaveplates each become increasingly fractured with a nonzero $\Delta\theta$ (Fig. 1*E*), producing a global circular birefringence response characterized by a rotation in polarization state. The magnitude of the circular birefringence, $\Delta\phi = \phi_{RCP} - \phi_{LCP}$, is given by:

$$\Delta\phi = -\frac{4\pi\Delta x}{\Lambda} \quad [1]$$

A detailed derivation of the circular birefringence response can be found in *SI Appendix*, section 3. We see that the circular birefringence modulation period is equal to half of the metagrating period, such that a full 2π rotation of the polarization state is achieved by incrementally increasing Δx up to $\Lambda/2$. The circular birefringence response derived in this simplified analysis is fully consistent with full-wave simulations of fractured full-nanowaveplate systems (*SI Appendix*, Fig. S3*D*).

Inspection of Eq. **1** reveals a number of notable properties of the system. First, circular birefrigence depends only on Δx and is independent of the spatial coordinate, x, indicating that the degree of symmetry breaking and corresponding accumulation of geometric phase in the metasurface system is constant across the system. This feature can be visualized on the Poincare spheres in Fig. 1 *D* and *E*, where the enclosed path area is constant for fractured full nanowaveplates at different positions along the metasurface system. Second, the modulation period for circular birefringence is inversely proportional to the metagrating period. As such, systems intended for tasks requiring more precise polarization control can be designed with larger periods that are more robust to misalignment, while those intended for high-speed modulation applications can be designed with smaller periods. Third, the circular birefringence response is completely independent of the wavelength of incident light, indicating that achromatic polarization control may be achieved as long as each nanowaveguide component functions as a half-waveplate.

Achromatic Optimization

To demonstrate our concept, we design, fabricate, and characterize sets of achromatic geometric phase metagratings, each configured with half-waveplate responses, operating at wavelengths ranging from 700 to 900 nm. These devices are fabricated from single crystal silicon films on glass because crystalline silicon has a high dielectric constant and nearly negligible absorption at our desired wavelength range (28). To ensure that the nanowaveplates support high transmission and a broadband response across our bandwidth of interest, we utilize topology optimization, which is a powerful tool for designing high-performance, free-form nanophotonic elements (11, 29–34). The optimization Figure of Merit is half-waveplate conversion efficiency, which is defined as the ratio of transmitted LCP to incident RCP intensity given an incident RCP wave. To impose achromatic behavior, the Figure of Merit is computed and averaged across nine different wavelengths. More details pertaining to the topology-optimization method are in *SI Appendix*, section 4.

The optimization trajectory of a successfully designed free-form half-nanowaveplate is shown in Fig. 2*A*. The optimization domain consists of an individual nanowaveguide structure with periodic boundary conditions along the lateral dimensions. The initial domain consists of a random grayscale permittivity distribution, and it gradually converges to a free-form silicon nanostructure with half-waveplate properties by the end of the optimization. The final topology-optimized nanowaveplate has a high conversion efficiency across the full 700- to 900-nm band (Fig. 2*B*) for all angular orientations (*SI Appendix*, Fig. S5*A*), with a bandwidth that is broader than that of rectangular nanowaveplates used in

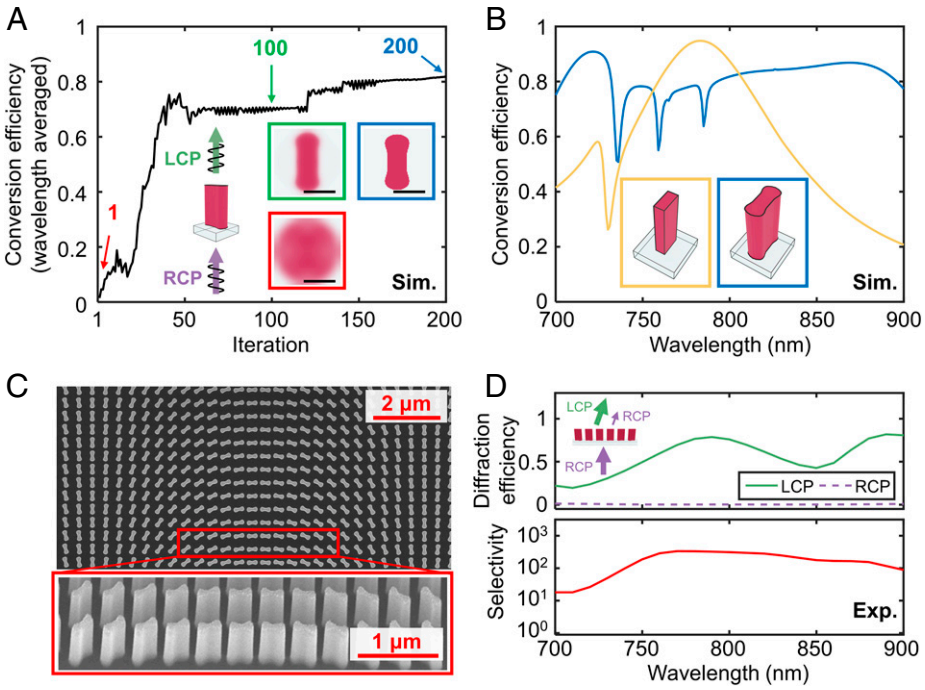

Fig. 2. Topology-optimized geometric phase nanowaveplates and metagratings. (*A*) Plot of conversion efficiency versus iteration number for the adjoint optimization of an individual half-waveplate nanowaveguide, averaged across the wavelength range 700 to 900 nm. (*A*, *Insets*) Top views of the nanowaveplate dielectric distribution at the 1st, 100th, and 200th iteration numbers. (Scale bar: 200 nm.) (*B*) Plot of the theoretical conversion efficiencies of half-nanowaveplates designed using topology optimization (blue) and a standard rectangular shape (orange). (*B*, *Insets*) Three-dimensional renderings of the nanowaveplate layouts. (*C*) Scanning electron micrograph (SEM) of the top view of a fabricated geometric phase metagrating comprising an array of topology-optimized half-nanowaveplates with a linear gradient in angular orientation. (*C*, *Inset*) SEM of a tilted view of the same device. (*D*) Experimentally measured diffraction efficiencies (*Upper*) and selectivities (*Lower*) of an individual metagrating, given an incident RCP wave. Exp., experimentally; Sim., simulated.

conventional geometric phase metasurfaces. A fullwave analysis of topology-optimized fractured full nanowaveplates shows that they uniquely exhibit nearly ideal geometric phase properties as a function of relative angle across our full band of interest, due to the high transmission efficiency of each half-nanowaveplate component (*SI Appendix*, Fig. S5*B*).

Device Fabrication

Each geometric phase metagrating is formed by specifying a periodic array of half-nanowaveplates, with each period featuring 25 nanowaveplates arranged with a gradual linear grading in angular orientation. To fabricate the devices, we first prepare crystalline silicon thin-film samples by bonding a silicon-on-insulator wafer onto a glass substrate and removing the silicon backside layer. The device pattern is defined in the film by using electron-beam lithography and reactive ion etching. More details on the fabrication process can be found in the *Materials and Methods* section. Scanning electron micrographs of the fabricated devices are shown in Fig. 2*C* and display good patterning fidelity and smooth, vertical sidewalls. Prior to optically characterizing the coupled metagrating system, we characterize the circular polarization response of individual metagratings, which should selectively diffract normally incident RCP and LCP light to the +1 and −1 orders, respectively. The experimentally measured diffraction efficiencies and diffraction selectivity, which is the ratio of transmitted RCP to LCP light in the +1 order given an incident RCP wave, is shown in Fig. 2*D*. The diffraction efficiencies are not as high as simulated values, likely due to fabrication imperfections, though they are relatively consistent as a function of wavelength and are higher than the theoretical efficiencies of standard geometric phase metagratings at long wavelengths (*SI Appendix*, Fig. S5). The selectivity is high across the full design bandwidth and sufficient for our application.

Optical Measurements

To set up our fractured metasurface system, we consider an alternative setup to that featured in Fig. 1 and align our metagrating pairs within a 4f system. The 4f setup is shown in Fig. 3*A* and serves as an optical relay that maps the output fields from the first metagrating to the lower interface of the second metagrating. Mechanistically, the first metagrating splits an incident linear-polarized beam into divergent RCP and LCP waves propagating into the +1 and −1 diffraction orders, respectively. The 4f system refocuses the beams to the second metagrating, where they recombine and transmit as a single beam to the zeroth diffraction order. The first metagrating position is set by using a linear translation stage while the second metagrating is held fixed. The relative displacement of the second metagrating imparts a relative phase shift to the recombined beams, leading to circular birefringence. While the metagratings are separated by large distances, the small relative displacements still dictate the symmetry and chiral properties of the system. In addition to simplifying metagrating alignment, our use of the 4f system also introduces two additional features. First, it eliminates near-field coupling effects within the fractured waveplates, removing parasitic effects from such coupling and enabling a continuous polarization rotation response from a continuous variation of Δx. Second, nondiffracted zeroth-order light from the first metagrating can be blocked, which improves the selectivity of the entire system. While our demonstration utilizes a 4f system, the concept can be adapted to alternative implementations that forgo the 4f system. In particular, integration of fractured waveplate metasurfaces with microelectromechanical systems (MEMS) would allow for ultracompact systems that support self-alignment between the metasurfaces and electrically controlled microscale motions. Dynamically tunable multilayer metasurfaces based on MEMS have been demonstrated for various applications (35, 36).

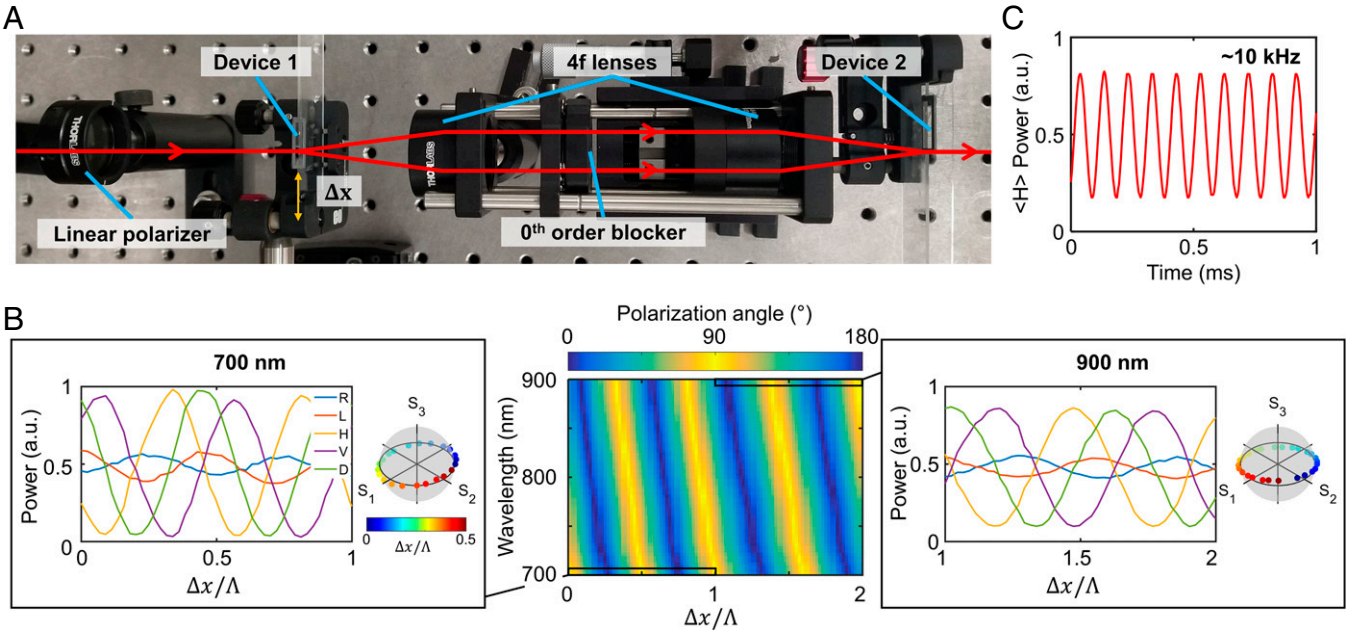

Fig. 3. Experimental characterization of reconfigurable metagrating system. (*A*) Top view of the experimental setup. The linearly polarized beam from the left is normally incident onto the first metagrating, which is mounted on a linear translation stage. The 4f lens system maps the transmitted fields onto the surface of the second metagrating, and the final outputted beam is inspected in a polarization analyzer. The beam blocker within the 4f system eliminates zeroth-order diffracted light from the first device. (*B*, *Center*) Contour plot showing the polarization angle of the outputted beam from the metagrating system as a function of Δx across the wavelength range of 700 to 900 nm. (*B*, *Left* and *Right*) Plots showing measured power of different polarization components of the outputted beam as a function of metagrating shear displacement. The left and right plots correspond to wavelengths of 700 nm and 900 nm, respectively. The fully polarized portion of each measurement is plotted on accompanying Poincare spheres for $\Delta x/\Lambda$ ranging from 0 to 0.5. (*C*) Plot of the horizontally polarized component of the output beam power over time for a metagrating shearing speed of 5 cm/s. The modulation speed is ∼10 kHz. a.u., arbitrary units.

Full polarization analysis of the fractured metasurface system is performed for a high-resolution scan in wavelength and Δx. The system is illuminated with horizontally polarized light, and the output horizontal, vertical, diagonal, and circular polarized components are measured at each wavelength and displacement position by using a polarization analyzer. From these measurements, the Stokes vector of the output light and orientation angle of its polarization state are readily computed. The measurements demonstrate tunable and achromatic polarization rotation resulting from circular birefringence in the system. Fig. 3 *B*, *Center* shows the linear polarization angle of the outgoing beam for Δx's spanning two metagrating periods, measured at 41 distinct wavelengths uniformly spaced within 700 to 900 nm. While some offset error is visible due to small misalignments in the setup, the polarization is consistently rotated across the entire bandwidth as the two gratings are displaced. The modulation period is half of the metagrating period, as predicted by our prior geometric phase analysis. The raw intensity values measured from the polarization analyzer at 700 nm and 900 nm are shown in Fig. 3 *B*, *Left* and *Right*, respectively, together with plots of the fully polarized portion of the Stokes vectors on Poincare spheres. The linear polarization curves exhibit sinusoidal variations with large peak-to-peak amplitudes, indicating the high quality of linear polarization conversion in the system. The circular polarization curves are mostly constant, with slight variations arising from misalignment in the system, and are consistent with a lack of circularly polarized light conversion, as expected from the system. *SI Appendix*, section 7 contains a more detailed analysis of misalignment and its effect on the polarization state.

The ability for our system to modulate circular birefringence with microscopic motions allows for high-speed polarization modulation using modest stage motion speeds. As a demonstration, we fix the input beam wavelength to be 750 nm, translate the first metagrating at a speed of 5 cm/s, and measure the intensity of the horizontally polarized component of the outputted beam using a fixed horizontal polarizer and an oscilloscope. The resulting intensity profile as a function of time is plotted in Fig. 3*C* and shows a linear polarization modulation rate of ∼10 kHz.

These modulation rates may be further increased through a combination of faster translation stages and smaller metagrating periods: 1-MHz tuning speeds can be achieved with a period of 2 μm and translation speeds of 2 m/s. These speeds are much faster than existing technologies used for broadband, large-aperture polarization rotation. Techniques based on liquid crystals (37, 38) operate with modulation speeds peaking at 1 kHz, and those utilizing bulk optics, such as waveplates or mirrors via the Vladimirskii–Rytov–Berry effect (39), have operating speeds closer to 100 Hz. We note that photo-elastic and electro-optic modulators can tune polarization rotation at speeds of 100 kHz and 100 MHz, respectively, for typical commercial devices. However, these technologies are not broadband because they are reliant on tunable birefringence effects, and electro-optic modulators have limited aperture size.

Conclusion

In summary, we have proposed and experimentally demonstrated a method for dynamically controlling Pancharatnam–Berry phase using a fractured Pancharatnam–Berry-phase metasurface system. Symmetry breaking imposed by microscopic displacements enables the tuning of the geometric phase response of the system, enabling arbitrary broadband circular birefringence responses with high fidelity and fast speeds in periodic metasurface systems. We anticipate that other modalities in active geometric phase modulation can be tailored in metasurface systems with combinations of translational and rotational movements and that richer functionalities will be enabled using metasurfaces with different underlying symmetry properties. Further variations in symmetry breaking can be achieved through the interplay between geometric and dynamical phase control. We envision that these concepts can extend to other domains beyond electromagnetics, including electronics, classical mechanics, and quantum mechanics, which support manifestations of geometric phase.

Materials and Methods

Topology Optimization. Topology optimization was utilized to design free-form geometric phase nanowaveguides operating as half-waveplates over the wavelength range 700 to 900 nm. We will first discuss the process for only a single wavelength and later consider broadband optimization. Electromagnetic simulations were performed by using the RCWA package Reticolo (40). During each iteration, a forward simulation was first performed with the device illuminated from the bottom, and we recorded the fields inside of the device under horizontally and vertically polarized light incidence. Then, an adjoint simulation was performed, where the device was illuminated from above, and again the fields inside the device were recorded. A Figure of Merit was calculated from the two fields and was averaged across nine evenly spaced wavelengths in the target range. More detailed consideration of the topology optimization can be found in *SI Appendix*, section 4.

Topology optimization was performed by using periodic boundary conditions, and to minimize parasitic near-field coupling effects between stitched nanowaveguides in the metagratings themselves, we randomly rotated the unit-cell layouts throughout the optimization process. Each iteration, the unit cell was rotated to a random angle, and the forward and adjoint simulations were performed on the rotated unit cell. Within the base (i.e., unrotated) unit cell pattern, *x* and *y* symmetry were both enforced.

Fabrication Methodology. All devices consisted of 500-nm-thick single-crystal silicon structures on a glass substrate. Single-crystal silicon was used to minimize absorption losses at our wavelength range of interest. A more detailed discussion of the use of crystalline silicon in metasurfaces can be found in ref. 28. To fabricate these devices, we bonded a silicon-on-insulator (SOI) wafer onto a borosilicate glass substrate. To prepare the glass substrate, a 6% hydrogen silesquioxane (HSQ) solution was first spun onto the wafer at 3,000 rpm and then prebaked under vacuum for 20 min. A piece of SOI wafer (SOITEC) with a 500-nm-thick device layer was placed, with the device layer face down, on the coated glass wafer and bonded using an Electronics Vision 501 Wafer Bonder with a pressure of 2,000 N at 400 °C for 1 h. The back-side silicon was removed by using a combination of back-side polishing and etching with SF_6. The buried oxide layer was removed by wet-etching in a 50:1 hydrofluoric acid solution. The patterns were defined by using electron-beam lithography with a Vistec VB300 100-KeV tool using 6% HSQ negative tone resist at 1,000 rpm, developed in 1% NaOH/4% NaCl for 4 min, and etched in a Oxford ICP etcher with a SF_6/C_4F_8 mixture.

Data Availability. All study data are available in the article main text, *SI Appendix*, and/or GitHub (https://github.com/jonfanlab/data-wang2022dynamic).

ACKNOWLEDGMENTS. Part of this work was performed at the nano@Stanford labs, which are supported by the NSF as part of the National Nanotechnology Coordinated Infrastructure under Award ECCS-1542152; and Stanford Nano Shared Facilities, supported by the NSF under Award ECCS-2026822. The authors acknowledge support from NASA under Award 80NSSC21K0220; the Air Force Office of Scientific Research (AFOSR) Multidisciplinary University Research Initiative under Award FA9550-16-1-0031; the AFOSR under Award FA9550-18-1-0070; and the Packard Fellowship Foundation. E.W.W. acknowledges support from the Stanford Graduate Fellowship. Work at the Molecular Foundry was supported by the Office of Science, Office of Basic Energy Sciences, of the US Department of Energy under Contract DE-AC02-05CH11231.

Author affiliations: [a]Department of Electrical Engineering, Stanford University, Stanford, CA 94305; and [b]Molecular Foundry, Lawrence Berkeley National Laboratory, Berkeley, CA 94720

1. J. Mun *et al.*, Electromagnetic chirality: From fundamentals to nontraditional chiroptical phenomena. *Light Sci. Appl.* **9**, 139 (2020).
2. N. Berova, K. Nakanishi, R. Woody, eds., *Circular Dichroism: Principles and Applications* (Wiley-VCH, New York, 2nd ed., 2000).
3. A. Y. Zhu *et al.*, Giant intrinsic chiro-optical activity in planar dielectric nanostructures. *Light Sci. Appl.* **7**, 17158 (2018).
4. Y. Zhao, M. A. Belkin, A. Alù, Twisted optical metamaterials for planarized ultrathin broadband circular polarizers. *Nat. Commun.* **3**, 870 (2012).
5. J. K. Gansel *et al.*, Gold helix photonic metamaterial as broadband circular polarizer. *Science* **325**, 1513–1515 (2009).
6. P. P. Wang, S. J. Yu, A. O. Govorov, M. Ouyang, Cooperative expression of atomic chirality in inorganic nanostructures. *Nat. Commun.* **8**, 14312 (2017).
7. Z. Liu *et al.*, Nano-kirigami with giant optical chirality. *Sci. Adv.* **4**, eaat4436 (2018).
8. T. Kan *et al.*, Enantiomeric switching of chiral metamaterial for terahertz polarization modulation employing vertically deformable MEMS spirals. *Nat. Commun.* **6**, 8422 (2015).
9. S. Zhang *et al.*, Photoinduced handedness switching in terahertz chiral metamolecules. *Nat. Commun.* **3**, 942 (2012).
10. X. Duan, S. Kamin, F. Sterl, H. Giessen, N. Liu, Hydrogen-regulated chiral nanoplasmonics. *Nano Lett.* **16**, 1462–1466 (2016).
11. Z. Shi *et al.*, Continuous angle-tunable birefringence with freeform metasurfaces for arbitrary polarization conversion. *Sci. Adv.* **6**, eaba3367 (2020).
12. C. Pfeiffer, C. Zhang, V. Ray, L. J. Guo, A. Grbic, Polarization rotation with ultra-thin bianisotropic metasurfaces. *Optica* **3**, 427 (2016).
13. A. V. Kildishev, A. Boltasseva, V. M. Shalaev, Planar photonics with metasurfaces. *Science* **339**, 1232009 (2013).
14. A. Overvig, N. Yu, A. Alù, Chiral quasi-bound states in the continuum. *Phys. Rev. Lett.* **126**, 073001 (2021).
15. Q. Song *et al.*, Bandwidth-unlimited polarization-maintaining metasurfaces. *Sci. Adv.* **7**, eabe1112 (2021).
16. M. Liu *et al.*, Broadband generation of perfect Poincaré beams via dielectric spin-multiplexed metasurface. *Nat. Commun.* **12**, 2230 (2021).
17. D. Lin, P. Fan, E. Hasman, M. L. Brongersma, Dielectric gradient metasurface optical elements. *Science* **345**, 298–302 (2014).
18. M. Khorasaninejad, K. B. Crozier, Silicon nanofin grating as a miniature chirality-distinguishing beam-splitter. *Nat. Commun.* **5**, 5386 (2014).
19. Q. Fan *et al.*, Independent amplitude control of arbitrary orthogonal states of polarization via dielectric metasurfaces. *Phys. Rev. Lett.* **125**, 267402 (2020).
20. K. Ou *et al.*, Mid-infrared polarization-controlled broadband achromatic metadevice. *Sci. Adv.* **6**, eabc0711 (2020).
21. E. Maguid *et al.*, Photonic spin-controlled multifunctional shared-aperture antenna array. *Science* **352**, 1202–1206 (2016).
22. A. H. Dorrah, N. A. Rubin, A. Zaidi, M. Tamagnone, F. Capasso, Metasurface optics for on-demand polarization transformations along the optical path. *Nat. Photonics* **15**, 287–296 (2021).
23. H. T. Chen *et al.*, A metamaterial solid-state terahertz phase modulator. *Nat. Photonics* **3**, 148–151 (2009).
24. N. A. Rubin *et al.*, Matrix Fourier optics enables a compact full-Stokes polarization camera. *Science* **365**, eaax1839 (2019).
25. A. S. Solntsev, G. S. Agarwal, Y. S. Kivshar, Metasurfaces for quantum photonics. *Nat. Photonics* **15**, 327–336 (2021).
26. M. Berry, The adiabatic phase and Pancharatnams phase for polarized light. *J. Mod. Opt.* **34**, 1401–1407 (1987).
27. E. Cohen *et al.*, Geometric phase from Aharonov–Bohm to Pancharatnam–Berry and beyond. *Nat. Rev. Phys* **1**, 437–449 (2019).
28. D. Sell, J. Yang, S. Doshay, K. Zhang, J. A. Fan, Visible light metasurfaces based on single-crystal silicon. *ACS Photonics* **3**, 1919–1925 (2016).
29. D. Sell, J. Yang, S. Doshay, R. Yang, J. A. Fan, Large-angle, multifunctional metagratings based on freeform multimode geometries. *Nano Lett.* **17**, 3752–3757 (2017).
30. D. Sell *et al.*, Ultra-high-efficiency anomalous refraction with dielectric metasurfaces. *ACS Photonics* **5**, 2402–2407 (2018).
31. S. Molesky *et al.*, Inverse design in nanophotonics. *Nat. Photonics* **12**, 659–670 (2018).
32. C. M. Lalau-Keraly, S. Bhargava, O. D. Miller, E. Yablonovitch, Adjoint shape optimization applied to electromagnetic design. *Opt. Express* **21**, 21693–21701 (2013).
33. N. Mohammadi Estakhri, B. Edwards, N. Engheta, Inverse-designed metastructures that solve equations. *Science* **363**, 1333–1338 (2019).
34. T. W. Hughes, M. Minkov, I. A. D. Williamson, S. Fan, Adjoint method and inverse design for nonlinear nanophotonic devices. *ACS Photonics* **5**, 4781–4787 (2018).
35. E. Arbabi *et al.*, MEMS-tunable dielectric metasurface lens. *Nat. Commun.* **9**, 812 (2018).
36. Z Han, S Colburn, A Majumdar, KF Bohringer, Millimeter-scale focal length tuning with mems-integrated meta-optics employing high-throughput fabrication. arXiv [Preprint] (2021). https://arxiv.org/abs/2111.07477 (Accessed 20 January 2022).
37. Z. Zhuang, Y. J. Kim, J. S. Patel, Achromatic linear polarization rotator using twisted nematic liquid crystals. *Appl. Phys. Lett.* **76**, 3995–3997 (2000).
38. D. Y. Guo *et al.*, Electrotunable achromatic polarization rotator. *Optica* **8**, 364 (2021).
39. N. I. Petrov, Achromatic polarization rotator. *Appl. Opt.* **46**, 6340–6343 (2007).
40. JP Hugonin, P Lalanne, *RETICOLO software for grating analysis*. arXiv [Preprint] (2021). https://arxiv.org/abs/2101.00901 (Accessed 1 December 2021).